

We are IntechOpen, the world's leading publisher of Open Access books Built by scientists, for scientists

6,900

Open access books available

185,000

International authors and editors

200M

Downloads

Our authors are among the

154

Countries delivered to

TOP 1%

most cited scientists

12.2%

Contributors from top 500 universities



WEB OF SCIENCE™

Selection of our books indexed in the Book Citation Index
in Web of Science™ Core Collection (BKCI)

Interested in publishing with us?
Contact book.department@intechopen.com

Numbers displayed above are based on latest data collected.
For more information visit www.intechopen.com



Hysteresis of Ceramic-Matrix Composites

Li Longbiao

Abstract

In this chapter, the hysteresis behavior of fiber-reinforced ceramic-matrix composites (CMCs) is investigated. Based on the interface slip state inside of CMCs, the hysteresis loops can be divided into four different cases. The relationship between the internal damage and the hysteresis loops of CMCs is established. Using the experimental hysteresis loops, the fiber/matrix interface frictional coefficient can be obtained. The mechanical hysteresis loops and the fiber/matrix interface frictional coefficient of SiC/CAS and C/SiC composites are predicted using the present models. When the fiber/matrix interface frictional coefficient decreases under cyclic fatigue loading, the fatigue hysteresis loops, fatigue hysteresis dissipated energy, fiber/matrix interface debonding, and slip all change. The fatigue hysteresis dissipated energy first increases and then decreases with decreasing interface frictional coefficient.

Keywords: ceramic-matrix composites (CMCs), hysteresis loops, matrix cracking, interface debonding

1. Introduction

Ceramic-matrix composites (CMCs) possess high specific strength and high specific modulus, corrosion, and wear resistance, especially at elevated temperature, and have already been applied on hot section components of commercial aero engine [1, 2].

Upon unloading and subsequent reloading, the fatigue hysteresis loops develop due to the frictional slip that occurred along any interface debonding region [3–6]. Kotil et al. [7] investigated the fatigue hysteresis loops of fiber-reinforced unidirectional CMCs with low and high fiber/matrix interface shear stress. The fatigue hysteresis loops' width decreases with increasing interface shear stress. Pryce and Smith [8] and Keith and Kedward [9] divided the fiber/matrix interface debonding into two cases of partial and complete debonding. Ahn and Curtin [10] investigated the effect of matrix stochastic cracking on the fatigue hysteresis loops of fiber-reinforced unidirectional CMCs. The matrix crack spacing was divided into three cases of long, medium, and short. Vagaggini et al. [11] investigated the fatigue hysteresis loops of fiber-reinforced unidirectional CMCs with weak and strong fiber/matrix interface bonding based on the Hutchinson-Jensen fiber pullout model [12]. Solti et al. [13] investigated the fatigue hysteresis loops of fiber-reinforced unidirectional CMCs when the interface was chemically bonded and partially debonded by adopting the maximum fiber/matrix interface shear strength criterion

to determine the fiber/matrix interface debonding length. Li et al. investigated the effects of the fiber/matrix interface debonding [14–16], fiber Poisson contraction [17], fiber fracture [18], and multiple matrix cracking [19] on the fatigue hysteresis loops of fiber-reinforced unidirectional and cross-ply CMCs when the interface was chemically bonded. The area associated with the fatigue hysteresis loops is the energy lost during corresponding unloading/reloading cycles [6]. The fiber/matrix interface shear stress within the debonding region affects the fatigue hysteresis energy lost, i.e., the size and shape of the fatigue hysteresis loops. Cho et al. [20] developed an approach to estimate the interface shear stress from the frictional heating measurements. Li et al. [21] developed an approach to estimate the fiber/matrix interface shear stress of fiber-reinforced unidirectional CMCs from fatigue hysteresis loss energy. However, due to the Poisson contraction effect, the fiber/matrix interface shear stress changes with unloading and reloading [22].

In this chapter, the fatigue hysteresis behavior of fiber-reinforced CMCs is investigated. The relationship between the internal damage and the fatigue hysteresis loops of fiber-reinforced CMCs is established. Using the experimental fatigue hysteresis loops, the fiber/matrix interface frictional coefficient can be obtained. The mechanical fatigue hysteresis loops and the fiber/matrix interface frictional coefficient of SiC/CAS and C/SiC composites are predicted.

2. Theoretical model

Upon loading to the fatigue peak stress, multiple damage mechanisms of the matrix cracking and fiber/matrix interface debonding occur. **Figure 1** shows the unit cell extracted from fiber-reinforced CMCs. The length of the unit cell is half of the matrix crack spacing of $l_c/2$, and the fiber/matrix interface debonding length is l_d . The fiber and the matrix radius are r_f and R .

Based on the fiber/matrix interface slip mechanism, the fatigue hysteresis loops of fiber-reinforced CMCs can be divided into four different cases, as the following:

1. Case I, the fiber complete sliding relative to the matrix in the partial debonding interface between the fiber and the matrix.
2. Case II, the fiber partial sliding relative to the matrix in the partial debonding interface between the fiber and the matrix.

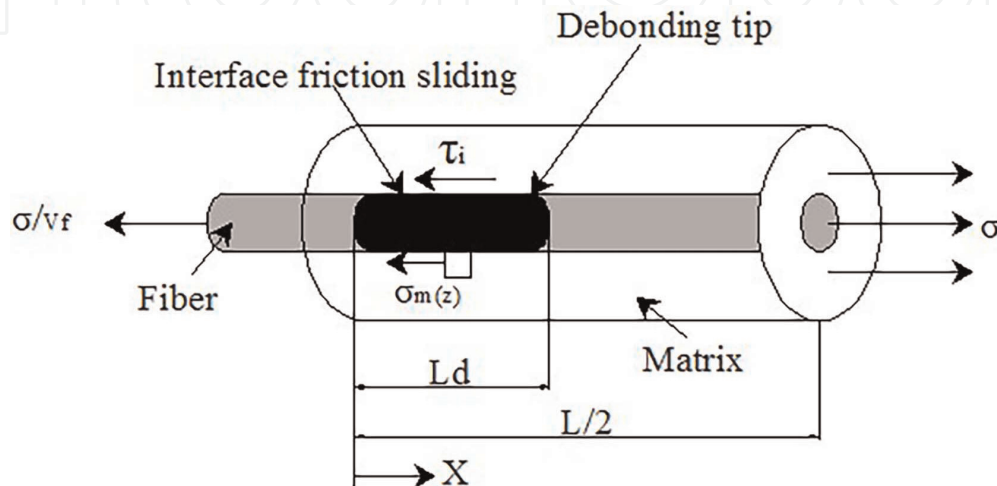


Figure 1.
The unit cell of composite.

3. Case III, the fiber partial sliding relative to the matrix in the complete debonding interface between the fiber and the matrix.
4. Case IV, the fiber complete sliding relative to the matrix in the complete debonding interface between the fiber and the matrix.

2.1 Case I

Upon unloading to the applied stress of σ (i.e., $\sigma_{\min} < \sigma < \sigma_{\max}$), the fiber/matrix interface debonding region can be divided into two regions of the interface counter slip region and interface slip region. When the applied stress is higher than the unloading transition stress of $\sigma > \sigma_{\text{tr_pu}}$, the fiber axial stress distribution upon unloading can be determined using the following equation:

$$\sigma_f(z) = \begin{cases} \frac{\sigma}{V_f} - \frac{\alpha v_f}{V_f(\alpha v_f + \gamma v_m)} (\bar{\sigma} - \sigma) (e^{-\lambda z} - 1), z \in [0, y] \\ \frac{\sigma}{V_f} - \frac{\alpha v_f}{V_f(\alpha v_f + \gamma v_m)} (\bar{\sigma} - \sigma) (e^{\lambda(z-2y)} - 1), z \in [y, l_d] \\ \left(\frac{\sigma}{V_f} - \frac{\alpha v_f (\bar{\sigma} - \sigma)}{V_f(\alpha v_f + \gamma v_m)} (e^{\lambda(l_d-2y)} - 1) - \sigma_{fo} \right) e^{-\frac{\rho(z-l_d)}{r_f}} + \sigma_{fo}, z \in \left[l_d, \frac{l_c}{2} \right] \end{cases} \quad (1)$$

where

$$y = \frac{1}{2} \left\{ l_d(\sigma_{\max}) - \frac{1}{\lambda} \ln \left[1 + \frac{(\alpha v_f + \gamma v_m)(\sigma - \sigma_0)}{\alpha v_f(1 + \beta)(\bar{\sigma} - \sigma)} \right] \right\} \quad (2)$$

When the applied stress is lower than the unloading transition stress of $\sigma_{\min} < \sigma < \sigma_{\text{tr_pu}}$, the fiber/matrix interface counter slip length occupies the entire interface debonding region, and the stress within the fiber can be determined using Eq. (1) by setting $y = l_d$.

Upon reloading to the applied stress of σ (i.e., $\sigma_{\min} < \sigma < \sigma_{\max}$), the fiber/matrix interface debonding region can be divided into three regions of new slip region, counter slip region, and slip region. When the applied stress is higher than the reloading transition stress of $\sigma < \sigma_{\text{tr_pr}}$, the fiber axial stress distribution upon reloading can be determined using the following equation:

$$\sigma_f(z) = \begin{cases} \frac{\sigma}{V_f} - \frac{\alpha v_f}{V_f(\alpha v_f + \gamma v_m)} (\bar{\sigma} - \sigma) (e^{\lambda z} - 1), z \in [0, z'] \\ \frac{\sigma}{V_f} - \frac{\alpha v_f}{V_f(\alpha v_f + \gamma v_m)} (\bar{\sigma} - \sigma) (e^{-\lambda(z-2z')} - 1), z \in [z', y] \\ \frac{\sigma}{V_f} - \frac{\alpha v_f}{V_f(\alpha v_f + \gamma v_m)} (\bar{\sigma} - \sigma) (e^{\lambda(z-2y+2z')} - 1), z \in [y, l_d] \\ \left(\frac{\sigma}{V_f} - \frac{\alpha v_f (\bar{\sigma} - \sigma)}{V_f(\alpha v_f + \gamma v_m)} (e^{\lambda(l_d-2y+2z')} - 1) - \sigma_{fo} \right) e^{-\frac{\rho(z-l_d)}{r_f}} + \sigma_{fo}, z \in [l_d, l_c/2] \end{cases} \quad (3)$$

where

$$z' = y(\sigma_{\min}) - \frac{1}{2} \left\{ l_d(\sigma_{\max}) - \frac{1}{\lambda} \ln \left[1 + \frac{(\alpha v_f + \gamma v_m)(\sigma - \sigma_0)}{\alpha v_f(\bar{\sigma} - \sigma)(1 + \beta)} \right] \right\} \quad (4)$$

When the applied stress is higher than the transition stress of $\sigma_{tr_pr} < \sigma < \sigma_{max}$, the new slip length occupies the entire interface debonding length, and the stress within the fiber can be determined using Eq. (3) by setting $z' = l_d$.

2.2 Case II

For the interface slip Case II, the fiber complete slides relative to the matrix in the partial debonding interface between the fiber and the matrix. The interface counter slip length y upon complete unloading is less than the interface debonding length of l_d , i.e., $y(\sigma_{min}) < l_d$. The fiber axial stress distribution can be determined by Eq. (1), and the interface counter slip length y is determined by Eq. (2). The new interface slip length of z' upon reloading to the peak stress of σ_{max} is less than the interface debonding length of l_d , i.e., $z'(\sigma_{max}) < l_d$. The fiber axial stress distribution is determined by Eq. (3); the new interface slip length z' is determined by Eq. (4).

2.3 Case III

For the interface slip Case III, the fiber partial slides relative to the matrix in the complete debonding interface between the fiber and the matrix. Upon complete unloading, the interface counter slip length of y is less than the half matrix crack space of $l_c/2$, i.e., $y(\sigma_{min}) < l_c/2$. The fiber axial stress distribution upon unloading can be determined using the following equation:

$$\sigma_f(z) = \begin{cases} \frac{\sigma}{V_f} - \frac{\alpha v_f}{V_f(\alpha v_f + \gamma v_m)} (\bar{\sigma} - \sigma) (e^{-\lambda z} - 1), z \in [0, y] \\ \frac{\sigma}{V_f} - \frac{\alpha v_f}{V_f(\alpha v_f + \gamma v_m)} (\bar{\sigma} - \sigma) (e^{\lambda(z-2y)} - 1), z \in [y, l_c/2] \end{cases} \quad (5)$$

where

$$y = \frac{1}{2\lambda} \ln \frac{\alpha v_f(1 + \beta)(\bar{\sigma} - \sigma)(\bar{\sigma} - \sigma_{max}) + (\alpha v_f + \gamma v_m)(\bar{\sigma} - \sigma)\sigma_{max}}{\alpha v_f(1 + \beta)(\bar{\sigma} - \sigma)(\bar{\sigma} - \sigma_{max}) + (\alpha v_f + \gamma v_m)(\bar{\sigma} - \sigma_{max})\sigma} \quad (6)$$

Upon reloading to the peak stress of σ_{max} , the interface new slip length of z' is less than the half matrix crack space of $l_c/2$, i.e., $z'(\sigma_{min}) < l_c/2$. The fiber axial stress distribution upon reloading can be determined using the following equation:

$$\sigma_f(z) = \begin{cases} \frac{\sigma}{V_f} - \frac{\alpha v_f}{V_f(\alpha v_f + \gamma v_m)} (\bar{\sigma} - \sigma) (e^{\lambda z} - 1), z \in [0, z'] \\ \frac{\sigma}{V_f} - \frac{\alpha v_f}{V_f(\alpha v_f + \gamma v_m)} (\bar{\sigma} - \sigma) (e^{-\lambda(z-2z')} - 1), z \in [z', y] \\ \frac{\sigma}{V_f} - \frac{\alpha v_f}{V_f(\alpha v_f + \gamma v_m)} (\bar{\sigma} - \sigma) (e^{\lambda(z-2y+2z')} - 1), z \in [y, l_c/2] \end{cases} \quad (7)$$

where

$$z' = \frac{1}{2\lambda} \ln \frac{\alpha v_f(1 + \beta)(\bar{\sigma} - \sigma)(\bar{\sigma} - \sigma_{max}) + (\alpha v_f + \gamma v_m)(\bar{\sigma} - \sigma_{max})\sigma}{\alpha v_f(1 + \beta)(\bar{\sigma} - \sigma_{min})(\bar{\sigma} - \sigma_{max}) + (\alpha v_f + \gamma v_m)(\bar{\sigma} - \sigma_{max})\sigma_{min}} \quad (8)$$

2.4 Case IV

For the interface slip Case IV, the fiber complete slides relative to the matrix in the complete debonding interface between the fiber and the matrix. Upon

unloading to the transition stress of σ_{tr_fu} , the interface counter slip length of y reaches the half matrix crack space of $l_c/2$. When the applied stress of $\sigma > \sigma_{tr_fu}$, the interface counter slip length y is less than the half matrix crack space of $l_c/2$. The fiber axial stress distribution is determined by Eq. (5), and the interface counter slip length y is determined by Eq. (6). When the applied stress is lower than the transition stress of $\sigma_{min} < \sigma < \sigma_{tr_fu}$, the interface counter slip occupies the entire matrix crack space, and the fiber axial stress distribution is determined by Eq. (5) by setting $y = l_c/2$.

Upon reloading to the transition stress of σ_{tr_fr} , the new interface slip length z' reaches the half matrix crack space of $l_c/2$. When $\sigma < \sigma_{tr_fr}$, the interface new slip length z' is less than the half matrix crack space $l_c/2$. The fiber axial stress distribution is determined by Eq. (7), and the interface new slip length z' is determined by Eq. (8). When the applied stress is higher than the transition stress of $\sigma_{tr_fr} < \sigma < \sigma_{max}$, new slip length occurs over the entire matrix crack space, and the fiber axial stress distribution is given by Eq. (7) by setting $z' = l_c/2$.

2.5 Hysteresis loops and hysteresis dissipated energy

For the interface slip Case II, the unloading and reloading stress–strain relationships are given by the following equation:

$$\begin{aligned} \varepsilon_{c_pu} = & \frac{\sigma}{V_f E_f} - \frac{2\alpha v_f (\bar{\sigma} - \sigma)}{\lambda V_f E_f l_c (\alpha v_f + \gamma v_m)} \left(1 - 2e^{-\lambda y} + e^{\lambda(l_d - 2y)} \right) \\ & + \frac{\alpha v_f (\bar{\sigma} - \sigma)}{V_f E_f (\alpha v_f + \gamma v_m)} \left[1 - e^{\lambda(l_d - 2y)} (1 - 2l_d/l_c) \right] \end{aligned} \quad (9)$$

$$\begin{aligned} \varepsilon_{c_pr} = & \frac{\sigma}{V_f E_f} - \frac{4\alpha v_f (\bar{\sigma} - \sigma)}{\lambda V_f E_f l_c (\alpha v_f + \gamma v_m)} \left(e^{\lambda z'} - e^{-\lambda(y - 2z')} + e^{\lambda(l_d - 2y + 2z')} - 1 \right) \\ & + \frac{\alpha v_f (\bar{\sigma} - \sigma)}{V_f E_f (\alpha v_f + \gamma v_m)} \left[1 - e^{\lambda(l_d - 2y + 2z')} (1 - 2l_d/l_c) \right] \end{aligned} \quad (10)$$

For the interface slip Case I, the unloading stress–strain relationship can be divided into two regions. When the applied stress is higher than the transition stress of $\sigma > \sigma_{tr_pu}$, the unloading strain is determined by Eq. (9), and when the applied stress is lower than the transition stress of $\sigma < \sigma_{tr_pu}$, the unloading strain is determined by Eq. (9) by setting $y = l_d$. The reloading stress–strain relationship is divided into two regions. When the applied stress is lower than the transition stress of $\sigma < \sigma_{tr_pr}$, the reloading strain is determined by Eq. (10), and when the applied stress is higher than the transition stress of $\sigma > \sigma_{tr_pr}$, the reloading strain is determined by Eq. (10) by setting $z' = l_d$.

For the interface slip Case III, the unloading and reloading stress–strain relationships are determined by the following equation:

$$\varepsilon_{c_fu} = \frac{\sigma}{V_f E_f} + \frac{\alpha v_f (\bar{\sigma} - \sigma)}{V_f E_f (\alpha v_f + \gamma v_m)} - \frac{2\alpha v_f (\bar{\sigma} - \sigma)}{\lambda V_f E_f l_c (\alpha v_f + \gamma v_m)} \left(1 - 2e^{-\lambda y} + e^{\lambda(l_c/2 - 2y)} \right) \quad (11)$$

$$\begin{aligned} \varepsilon_{c_fr} = & \frac{\sigma}{V_f E_f} + \frac{\alpha v_f (\bar{\sigma} - \sigma)}{V_f E_f (\alpha v_f + \gamma v_m)} \\ & - \frac{2\alpha v_f (\bar{\sigma} - \sigma)}{\lambda V_f E_f l_c (\alpha v_f + \gamma v_m)} \left(2e^{\lambda z'} - 2e^{-\lambda(y - 2z')} + e^{\lambda(l_c/2 - 2y + 2z')} - 1 \right) \end{aligned} \quad (12)$$

For the interface slip Case IV, the unloading stress–strain relationship is divided into two regions. When the applied stress is higher than the transition stress of $\sigma > \sigma_{tr_fu}$, the unloading strain is determined by Eq. (11), and when the applied stress is lower than the transition stress of $\sigma < \sigma_{tr_fu}$, the unloading strain is determined by Eq. (11) by setting $y = l_c/2$. The reloading stress–strain relationship is divided into two regions. When the applied stress is lower than the transition stress of $\sigma < \sigma_{tr_fr}$, the reloading strain is determined by Eq. (12); when the applied stress is higher than the transition stress of $\sigma > \sigma_{tr_fr}$, the reloading strain is determined by Eq. (12) by setting $z' = l_c/2$.

Under cyclic fatigue loading, the area associated with the fatigue hysteresis loops is the energy lost during the corresponding cycle, which is defined by the following equation:

$$U = \int_{\sigma_{min}}^{\sigma_{max}} [\varepsilon_{cu}(\sigma) - \varepsilon_{cr}(\sigma)] d\sigma \quad (13)$$

3. Result and discussion

The experimental and predicted fatigue hysteresis loops and interface slip of fiber-reinforced unidirectional SiC/CAS composite under the fatigue peak stress of $\sigma_{max} = 185$ MPa are shown in **Figure 2**. Upon unloading and reloading, the unloading interface counter slip length approaches the interface debonding length at the unloading transition stress, and the reloading interface new slip length approaches the interface debonding length at the reloading transition stress. The fatigue unloading/reloading hysteresis loops under $\sigma_{max} = 185$ MPa correspond to the interface slip Case I.

The experimental and predicted fatigue hysteresis loops and interface slip of fiber-reinforced unidirectional SiC/CAS composite under the fatigue peak stress of $\sigma_{max} = 242$ MPa are shown in **Figure 3**. Upon unloading and reloading, the unloading interface counter slip length and the reloading interface new slip length do not approach the interface debonding length. The fatigue hysteresis loops under the fatigue peak stress of $\sigma_{max} = 242$ MPa correspond to the interface slip Case II.

The experimental and predicted fatigue hysteresis loop and interface slip of fiber-reinforced unidirectional SiC/CAS composite under the fatigue peak stress of $\sigma_{max} = 300$ MPa are shown in **Figure 4**. The interface partial debonds and the fiber partial slides upon unloading and reloading. The unloading interface counter slip length and reloading interface new slip length do not approach the interface debonding length. The fatigue hysteresis loops under the fatigue peak stress of $\sigma_{max} = 300$ MPa correspond to the interface slip Case III.

The experimental and predicted fatigue hysteresis loops and interface slip of SiC/CAS composite under the fatigue peak stress of $\sigma_{max} = 350$ MPa are shown in **Figure 5**. The interface complete debonds and the fiber complete slides upon unloading and reloading. The unloading interface counter slip length and the new interface slip length upon reloading approach the interface debonding length. The fatigue hysteresis loops under the fatigue peak stress of $\sigma_{max} = 350$ MPa correspond to the interface slip Case IV.

The fatigue hysteresis loops as a function of the fiber/matrix interface frictional coefficient of fiber-reinforced unidirectional SiC/CAS composite under the fatigue peak stress of $\sigma_{max} = 185$ MPa are shown in **Figure 6(a)**. The fatigue hysteresis dissipated energy as a function of the fiber/matrix interface frictional coefficient of fiber-reinforced unidirectional SiC/CAS composite is shown in **Figure 6(b)**. When the interface frictional coefficient is $\mu = 0.05 \sim 0.3$, the fatigue hysteresis dissipated energy increases with the decreasing fiber/matrix interface frictional coefficient, and the interface partial debonds ($l_d < l_c/2$ in **Figure 6(c)**), and the fiber complete

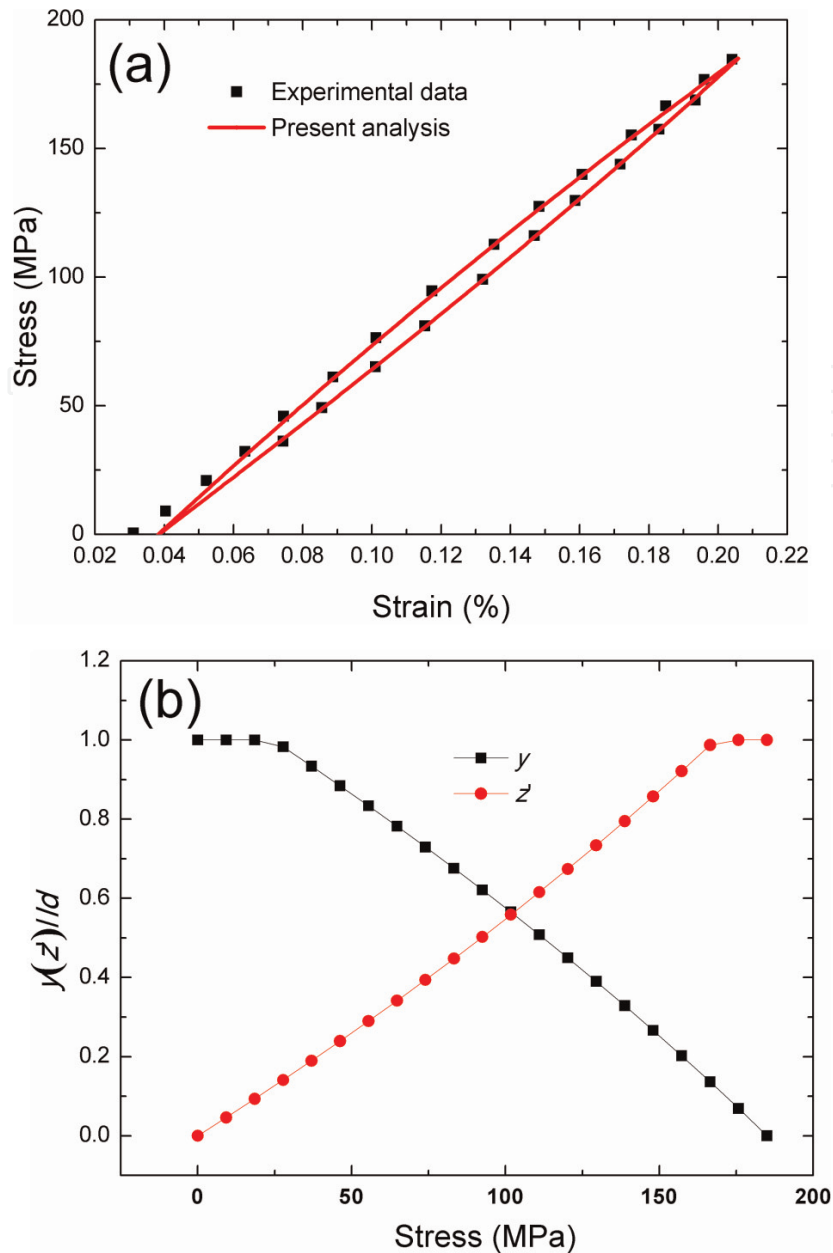


Figure 2. (a) The experimental and predicted fatigue hysteresis loops and (b) the fiber/matrix interface counter slip length and the interface new slip length versus the applied stress of fiber-reinforced unidirectional SiC/CAS composite under the fatigue peak stress of $\sigma_{max} = 185$ MPa.

slides relative to the matrix in the interface debonding region (i.e., $y(\sigma_{min}) = l_d$ in **Figure 6(d)**). The fatigue hysteresis loops correspond to the interface slip Case I. When the fiber/matrix interface frictional coefficient is $\mu = 0.01 \sim 0.05$, the fatigue hysteresis dissipated energy increases to the peak value and decreases with the decreasing interface frictional coefficient, and the interface complete debonds ($l_d = l_c/2$ in **Figure 6(c)**), and the fiber complete slides relative to the matrix in the interface debonding region ($y(\sigma_{min}) = l_d$ in **Figure 6(d)**). The fatigue hysteresis loops correspond to the interface slip Case IV.

4. Experimental comparison

The fatigue hysteresis loops, fatigue hysteresis dissipated energy, and interface slip of unidirectional C/SiC composite at room and elevated temperatures corresponding to different number of applied cycles are analyzed.

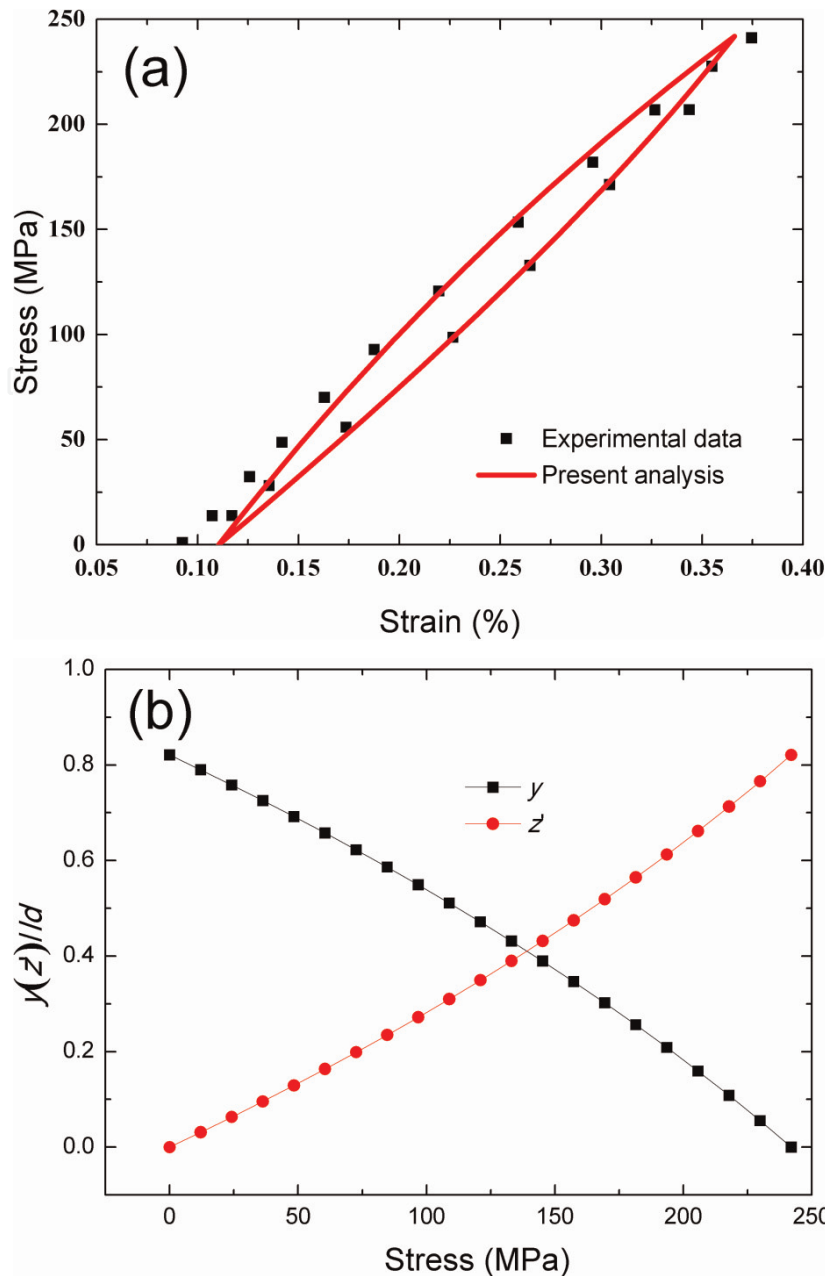


Figure 3. (a) The experimental and predicted fatigue hysteresis loops and (b) the fiber/matrix interface counter slip length and the interface new slip length versus the applied stress of fiber-reinforced unidirectional SiC/CAS composite under the fatigue peak stress of $\sigma_{max} = 242$ MPa.

4.1 Room temperature

The fatigue hysteresis dissipated energy as a function of the fiber/matrix interface frictional coefficient of C/SiC composite under the fatigue peak stress of $\sigma_{max} = 140$ MPa is shown in **Figure 7**. The fatigue hysteresis dissipated energy increases with decreasing fiber/matrix interface frictional coefficient to the peak value of $U = 22$ kJ/m³ and then decreases with the fiber/matrix interface frictional coefficient to $U =$ zero kJ/m³. The experimental fatigue hysteresis dissipated energy is $U = 18, 7.7, 6.5, 6.1, 4.2, 4, 3.8,$ and 3.4 kJ/m³ corresponding to $N = 1, 15, 155, 58, 804, 139, 326, 234, 783, 665, 129, 816, 908,$ and $1, 005, 541,$ respectively; the corresponding fiber/matrix interface frictional coefficient is $\mu = 1.1 \times 10^{-2}, 1.5 \times 10^{-3}, 1.3 \times 10^{-3}, 1.1 \times 10^{-3}, 8.4 \times 10^{-4}, 8 \times 10^{-4}, 7.5 \times 10^{-4},$ and $6.8 \times 10^{-4},$ respectively. Under the fatigue peak stress of $\sigma_{max} = 140$ MPa, the fatigue hysteresis

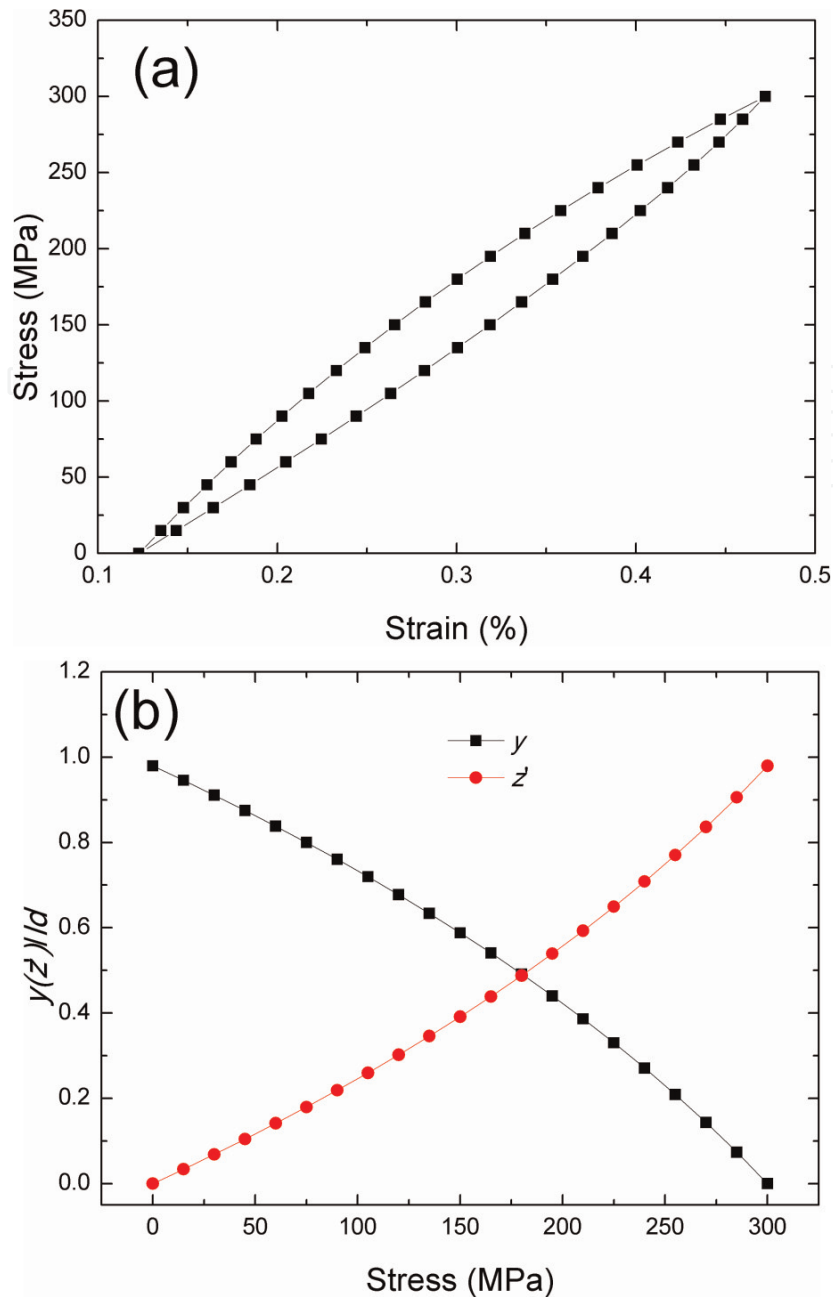


Figure 4.
 (a) The experimental and predicted fatigue hysteresis loops and (b) the interface counter slip length and the interface new slip length versus the applied stress of fiber-reinforced unidirectional SiC/CAS composite under the fatigue peak stress of $\sigma_{max} = 300$ MPa.

dissipated energy at $N = 1$ lies in the right part of the fatigue hysteresis dissipated energy versus the fiber/matrix interface frictional coefficient curve. The fatigue hysteresis loops at $N = 1$ correspond to the interface slip Case II. When the applied cycles increase, the fiber/matrix interface frictional coefficient decreases. The fatigue hysteresis loops at $N = 15, 155$ correspond to the interface slip Case IV.

4.2 Elevated temperature

The fatigue hysteresis dissipated energy as a function of the fiber/matrix interface frictional coefficient under the fatigue peak stress of $\sigma_{max} = 180$ MPa is shown in **Figure 8**. The fatigue hysteresis dissipated energy first increases with decreasing interface frictional coefficient to the peak value of $U = 36.5$ kJ/m³ and then

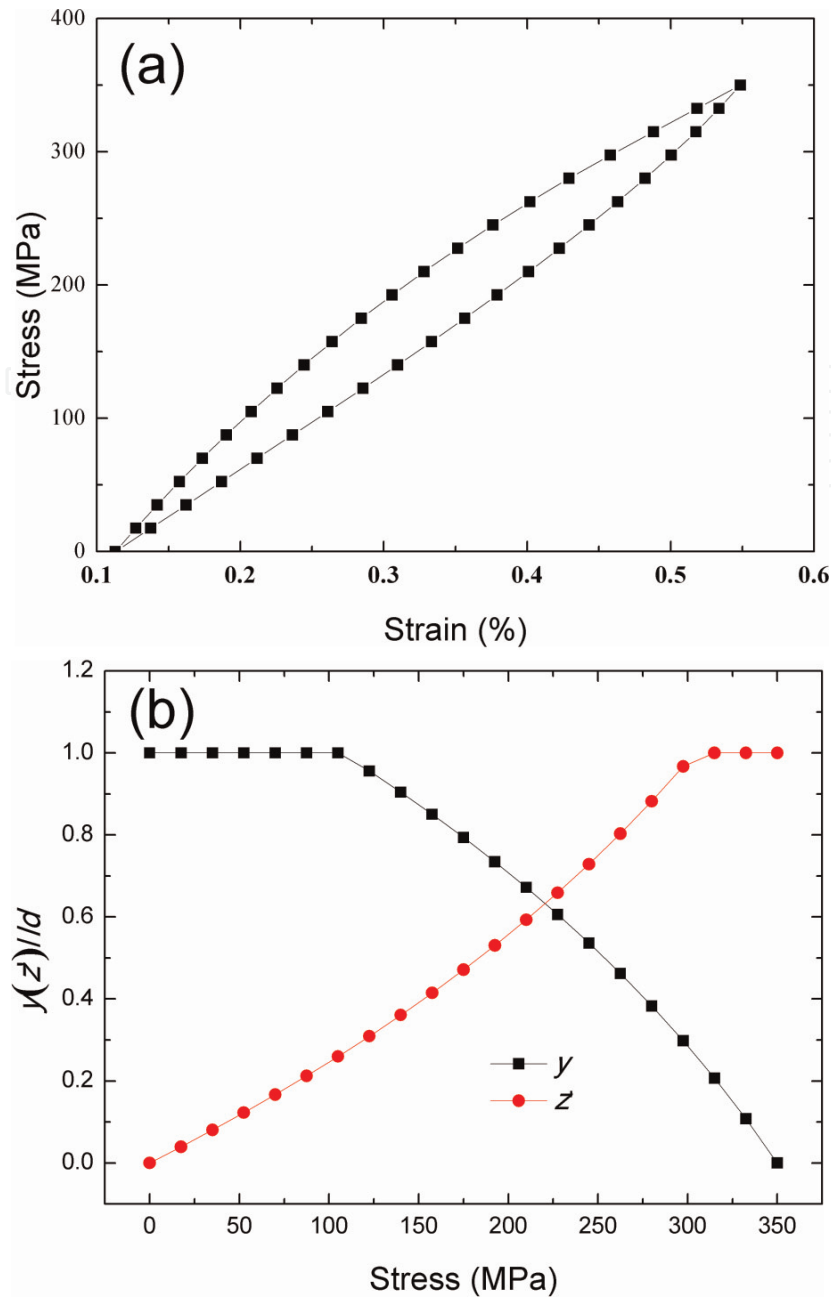


Figure 5.

(a) The experimental and predicted fatigue hysteresis loops and (b) the interface counter slip length and the interface new slip length versus the applied stress of fiber-reinforced unidirectional SiC/CAS composite under the fatigue peak stress of $\sigma_{max} = 350$ MPa.

decreases with the interface frictional coefficient to $U = \text{zero kJ/m}^3$. The experimental fatigue hysteresis dissipated energy is $U = 30, 22, 15, 9.8, 9.3, 8.7, 8, 7.5, 6.9, 6.7, 6.1, 6,$ and 5.8 kJ/m^3 , corresponding to $N = 1, 5, 10, 100, 1000, 8000, 21,000, 36,000, 55,000, 65,000, 75,000, 85,000,$ and $87,000$, respectively; the corresponding fiber/matrix interface frictional coefficient is $\mu = 1.1 \times 10^{-2}, 2.7 \times 10^{-3}, 1.8 \times 10^{-3}, 1.2 \times 10^{-3}, 1.1 \times 10^{-3}, 1 \times 10^{-3}, 9 \times 10^{-4}, 8.5 \times 10^{-4}, 8 \times 10^{-4}, 7.8 \times 10^{-4}, 5.1 \times 10^{-4}, 5 \times 10^{-4},$ and 4.9×10^{-4} , respectively. Under the fatigue peak stress of $\sigma_{max} = 180$ MPa, the fatigue hysteresis dissipated energy at $N = 1$ lies in the right part of the fatigue hysteresis dissipated energy versus the interface frictional coefficient curve. The fatigue hysteresis loops at $N = 1$ correspond to the interface slip Case II. When the applied cycles increase, the fiber/matrix interface frictional coefficient decreases due to the oxidation of the interphase. The fatigue hysteresis loops at $N = 5$ correspond to the interface slip Case IV.

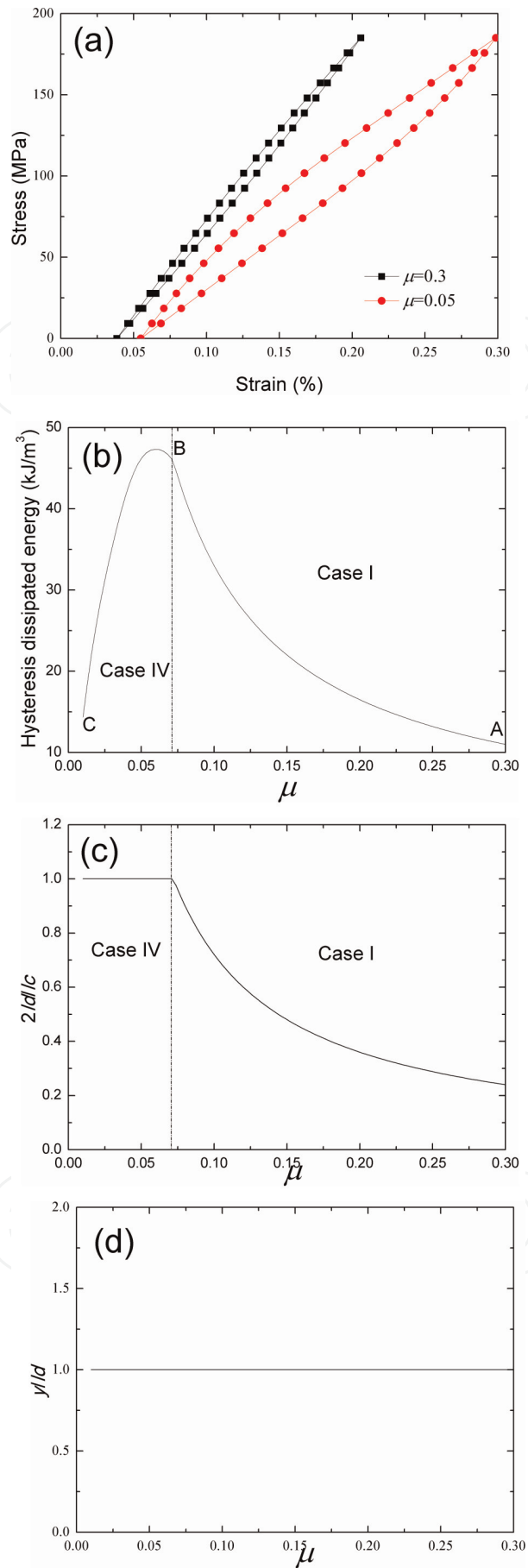


Figure 6. (a) The fatigue hysteresis loops corresponding to different fiber/matrix interfacial frictional coefficient; (b) the fatigue hysteresis dissipated energy versus the fiber/matrix interfacial frictional coefficient curves; (c) the interface debonding length versus the interfacial frictional coefficient curves; and (d) the interface counter slip length versus the interfacial frictional coefficient curves of fiber-reinforced unidirectional SiC/CAS composite under the fatigue peak stress of $\sigma_{max} = 185$ MPa.

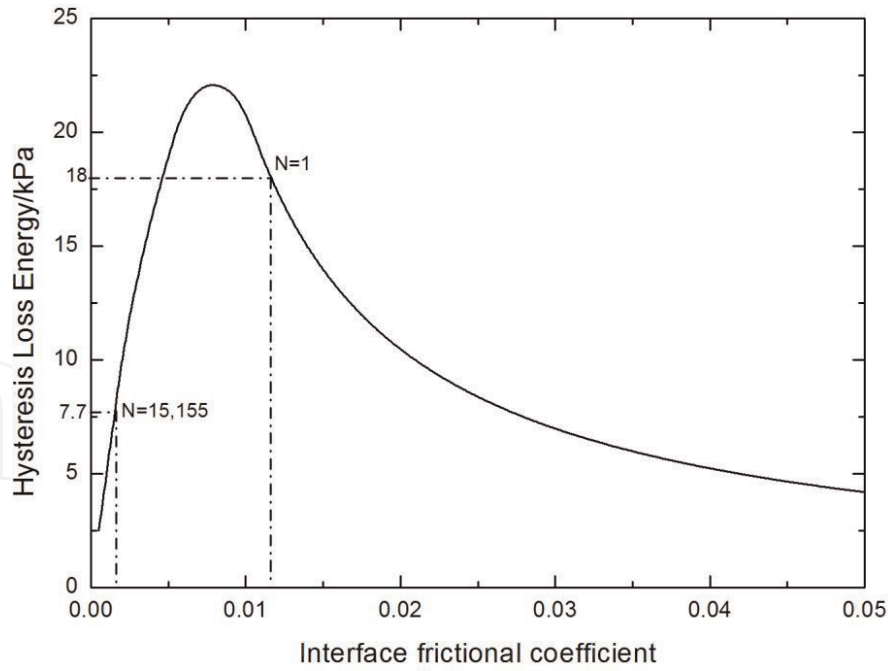


Figure 7. The experimental and predicted fatigue hysteresis dissipated energy versus the fiber/matrix interface frictional coefficient of fiber-reinforced unidirectional C/SiC composite under the fatigue peak stress of $\sigma_{max} = 140$ MPa at room temperature.

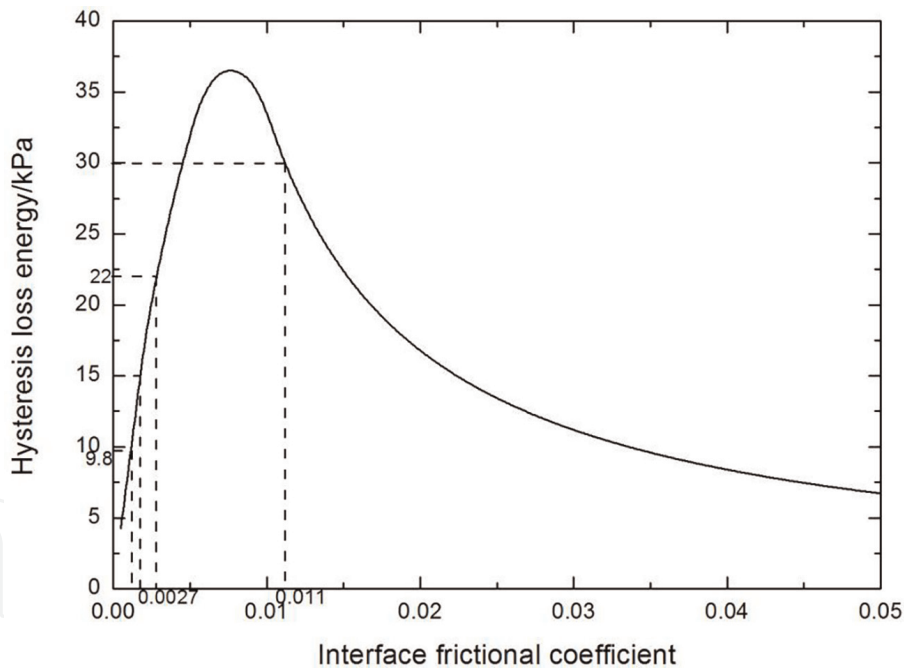


Figure 8. The experimental and predicted fatigue hysteresis dissipated energy versus the fiber/matrix interface frictional coefficient of fiber-reinforced unidirectional C/SiC composite under the fatigue peak stress of $\sigma_{max} = 180$ MPa at 800°C in air atmosphere.

5. Conclusion

In this chapter, the fatigue hysteresis behavior of fiber-reinforced CMCs was investigated. The relationship between the internal damage and the fatigue hysteresis loops of fiber-reinforced CMCs was established. Using the experimental fatigue hysteresis loops, the fiber/matrix interface frictional coefficient corresponding to different applied cycles can be obtained. The mechanical fatigue hysteresis loops

and the fiber/matrix interface frictional coefficient of SiC/CAS and C/SiC composites were predicted. The fatigue hysteresis loops of fiber-reinforced CMCs can be divided into four different cases, as the following:

1. Case I, the fiber complete sliding relative to the matrix in the partial debonding interface between the fiber and the matrix.
2. Case II, the fiber partial sliding relative to the matrix in the partial debonding interface between the fiber and the matrix.
3. Case III, the fiber partial sliding relative to the matrix in the complete debonding interface between the fiber and the matrix.
4. Case IV, the fiber complete sliding relative to the matrix in the complete debonding interface between the fiber and the matrix.

Acknowledgements

The work reported here is supported by the Fundamental Research Funds for the Central Universities (Grant No. NS2019038).

Author details

Li Longbiao
College of Civil Aviation, Nanjing University of Aeronautics and Astronautics,
Nanjing, China

*Address all correspondence to: llb451@nuaa.edu.cn

IntechOpen

© 2019 The Author(s). Licensee IntechOpen. Distributed under the terms of the Creative Commons Attribution - NonCommercial 4.0 License (<https://creativecommons.org/licenses/by-nc/4.0/>), which permits use, distribution and reproduction for non-commercial purposes, provided the original is properly cited. 

References

- [1] Li L. *Damage, Fracture and Fatigue of Ceramic-Matrix Composites*. Singapore: Springer Nature Singapore Pte Ltd.; 2018. DOI: 10.1007/978-981-13-1783-5. ISBN: 978-981-13-1782-8
- [2] Li L. *Thermomechanical Fatigue of Ceramic-Matrix Composites*. New Jersey, United States: Wiley-VCH; 2019. Available from: <https://onlinelibrary.wiley.com/doi/book/10.1002/9783527822614>. ISBN: 978-3-527-34637-0
- [3] Li L. Synergistic effects of temperature, oxidation, loading frequency and stress-rupture on damage evolution of cross-ply ceramic-matrix composites under cyclic fatigue loading at elevated temperatures in oxidizing atmosphere. *Engineering Fracture Mechanics*. 2017;**175**:15-30
- [4] Li L. Synergistic effects of stress-rupture and cyclic loading on strain response of fiber-reinforced ceramic-matrix composites at elevated temperature in oxidizing atmosphere. *Materials*. 2017;**10**:182
- [5] Li L. Damage evolution of cross-ply ceramic-matrix composites under stress-rupture and cyclic loading at elevated temperatures in oxidizing atmosphere. *Materials Science and Engineering A*. 2017;**688**:315-321
- [6] Fantozzi G, Reynaud P. Mechanical hysteresis in ceramic matrix composites. *Materials Science and Engineering A*. 2009;**521-522**:18-23
- [7] Kotil T, Holmes JW, Comninou M. Origin of hysteresis observed during fatigue of ceramic-matrix composites. *Journal of the American Ceramic Society*. 1990;**73**:1879-1883
- [8] Pryce AW, Smith PA. Matrix cracking in unidirectional ceramic matrix composites under quasi-static and cyclic loading. *Acta Metallurgica et Materialia*. 1993;**41**:1269-1281
- [9] Keith WP, Kedward KT. The stress-strain behavior of a porous unidirectional ceramic matrix composite. *Composites*. 1995;**26**:163-174
- [10] Ahn BK, Curtin WA. Strain and hysteresis by stochastic matrix cracking in ceramic matrix composites. *Journal of the Mechanics and Physics of Solids*. 1997;**45**:177-209
- [11] Vagaggini E, Domergue JM, Evans AG. Relationships between hysteresis measurements and the constituent properties of ceramic matrix composites: I, theory. *Journal of the American Ceramic Society*. 1995;**78**: 2709-2720
- [12] Hutchison JW, Jensen HM. Models of fiber debonding and pullout in brittle composites with friction. *Mechanics of Materials*. 1990;**9**:139-163
- [13] Solti JP, Robertson DD, Mall S. Estimation of interfacial properties from hysteresis energy loss in unidirectional ceramic matrix composites. *Advanced Composite Materials*. 2000;**9**(3):161-173
- [14] Li L. Modeling for cyclic loading/unloading hysteresis loops of carbon fiber-reinforced ceramic-matrix composites at room and elevated temperatures. Part I: Theoretical analysis. *Engineering Fracture Mechanics*. 2016;**164**:117-136
- [15] Li L. Modeling for cyclic loading/unloading hysteresis loops of carbon fiber-reinforced ceramic-matrix composites at room and elevated temperatures. Part II: Experimental comparisons. *Engineering Fracture Mechanics*. 2016;**164**:137-154

[16] Li L. Hysteresis loops of carbon fiber-reinforced ceramic-matrix composites with different fiber preforms. *Ceramics International*. 2016; **42**:16535-16551

[17] Li L, Song Y. Estimate interface frictional coefficient of ceramic matrix composites from hysteresis loops. *Journal of Composite Materials*. 2011; **45**: 989-1006

[18] Li L, Song Y, Sun Y. Modeling loading/unloading hysteresis behavior of unidirectional C/SiC ceramic matrix composites. *Applied Composite Materials*. 2013; **20**:655-672

[19] Li L. Fatigue hysteresis behavior of cross-ply C/SiC ceramic matrix composites at room and elevated temperatures. *Materials Science and Engineering A*. 2013; **586**:160-170

[20] Cho C, Holmes JW, Barber JR. Estimation of interfacial shear in ceramic composites from frictional heating measurements. *Journal of the American Ceramic Society*. 1991; **74**: 2802-2808

[21] Li L. Assessment of the interfacial properties from fatigue hysteresis loss energy in ceramic-matrix composites with different fiber preforms at room and elevated temperatures. *Materials Science and Engineering A*. 2014; **613**: 17-36

[22] Li L. Fatigue hysteresis behavior of unidirectional C/SiC ceramic matrix composites at room and elevated temperatures. *Materials Science and Engineering A*. 2015; **625**:1-18